Shape of the Q band in the absorption spectra of porphyrin nanotubes

Stradomska, Anna; Knoester, Jasper

Published in:
Journal of Chemical Physics

DOI:
10.1063/1.3481654

Shape of the *Q* band in the absorption spectra of porphyrin nanotubes: Vibronic coupling or exciton effects?

Anna Stradomska[a] and Jasper Knoester
Zernike Institute for Advanced Materials, University of Groningen, Nijenborgh 4, AG Groningen 9747, The Netherlands

(Received 20 April 2010; accepted 2 August 2010; published online 1 September 2010)

Absorption and linear dichroism spectra of self-assembled tubular aggregates of $TPPS_4$ porphyrin are studied theoretically with special emphasis on the low energy part of the spectra (the *Q* band region) where the coupling with intramolecular vibrations is pronounced. The model Hamiltonian includes both the excitonic coupling between four molecular electronic excited states contributing to the porphyrin *Q* and *B* bands as well as the intermediate-strength linear exciton-phonon coupling to one effective high-frequency molecular vibrational mode. Good agreement between the calculated and experimental spectra is obtained. The results allow us to identify the nature of the peaks observed in the *Q* band region of the aggregate's absorption spectrum; we show that the two most prominent peaks within the *Q* band originate from two different excitonic subbands. It is shown that the coupling between the *Q* and *B* bands plays an important role and the vibronic coupling affects the details of the absorption lineshape. © *2010 American Institute of Physics*.
[doi:10.1063/1.3481654]

I. INTRODUCTION

Self-assembled tubular aggregates of π-conjugated molecules[1–18] have recently attracted attention because of their structural similarities to photosynthetic antenna systems (chlorosomes) of green bacteria,[19] as well as their unique linear and nonlinear optical properties,[2,10] effective excitation energy transport,[5,12] and photoconductivity.[7,11] Their potential applications for artificial light-harvesting, optoelectronics, and energy transport make them attractive from the practical perspective. They are also interesting from a fundamental point of view, as systems to study the nature and dynamics of excited states in molecular assemblies of reduced dimensionality, as well as models for understanding the photophysics of natural light-harvesting complexes. A better insight into how the structure of the aggregate, the properties of the molecular building blocks, and the intermolecular interactions influence the photophysics and energy transport phenomena in such systems will guide the way for fine-tuning those materials for specific applications.

Among the tubular aggregates, those formed as a result of self-assembly of porphyrin derivatives, such as tetra(4-sulfonatophenyl)porphyrin ($TPPS_4$), take a prominent place because of their high stability and the reproducibility of their structural and optical properties. $TPPS_4$ dye forms aggregates in highly acidic water solutions. In neutral and basic solutions $TPPS_4$ has four negatively charged sulfonate groups (Fig. 1) and the electrostatic repulsion prevents aggregation. Upon increasing the acidity two protons are bound to the inner pyrrole nitrogen atoms forming the porphyrin diacid. The presence of these two protons induces a strong, saddle-type distortion of the porphyrin ring, as confirmed by DFT calculations[20] and crystallographic data for salts of similar porphyrins.[21,22] Further increase of pH results in two additional protons being bound to two of the sulfonate groups, forming a zwitterionic species (Fig. 1) that self-assemble into tubular aggregates, stabilized by Coulomb and $\pi-\pi$ interactions.

The aggregation is accompanied by a considerable change in optical spectra.[18] The monomer absorption spectrum (Fig. 2) exhibits two bands—the *B* band at 2.86 eV (434 nm) originates from a pair of degenerate electronic transitions B_x and B_y; similarly, the *Q* band absorption around 1.92 eV (645 nm) is due to another pair of (almost) degenerate transitions Q_x and Q_y (Ref. 20) (*x* and *y* denote the perpendicular orientations of the electronic transition dipole moments within the molecule as shown in Fig. 3). The *Q* band region clearly exhibits vibronic structure. Upon aggregation the monomeric absorption bands are split and shifted.[18] In particular, the *B* band is split into a very narrow redshifted peak at 2.53 eV (490 nm) and a wider peak at 2.93 eV (423 nm); the *Q* band is also redshifted by about 0.17 eV and the spacings between the peaks within this band are changed (Fig. 2).

The *B* band region of the absorption and linear dichorism (LD) spectra of $TPPS_4$ aggregates has been successfully modeled with an approach taking into account only the excitonic couplings within the *B* and *Q* bands and disregarding vibronic effects.[18] However, the shape of the *Q* band absorption could not be addressed within such a simple model. The apparent progressionlike shape of the monomer (and aggregate) spectrum (see Fig. 2) suggests that the coupling to high-frequency molecular vibrations may play an important role for this system. Modeling of the optical spectra of $TPPS_4$ nanotubes thus requires a theory that will account for both excitonic effects as well as the intermediate-strength coupling with molecular vibrations. In this paper we present

[a]Electronic mail: a.u.stradomska@rug.nl.

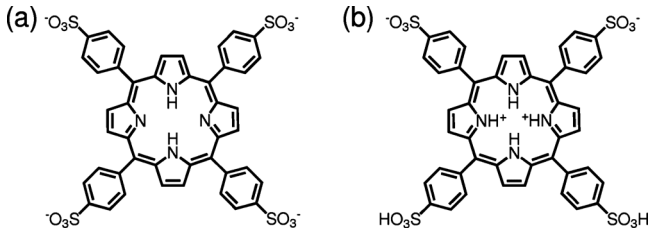

FIG. 1. $TPPS_4$ monomer (a) in pH=7 solution (b) in pH=1 solution.

a theoretical method that combines the description of excitons in cylindrical aggregates by Knoester and co-workers[18,23] with the two-particle approximation for the vibronic coupling introduced by Philpott[24] and used recently for molecular aggregates[25–27] and crystals.[28,29] This method goes beyond the perturbative limits of strong and weak vibronic coupling, and applied to tubular aggregates of $TPPS_4$ allows us to interpret the Q band region in their optical spectra. Surprisingly, we find that the main structure in the Q band region does not originate from vibronic coupling, but rather from a splitting in electronic subbands and the tubular geometry of the aggregate. The coupling between the Q and B bands turns out to be essential to understand the energy splitting between the main peaks in the Q band region.

This paper is organized as follows. In Sec. II, the model of the aggregate geometry, the vibronic Hamiltonian, and the two-particle approximation used for modeling the optical spectra of $TPPS_4$ aggregates are introduced. Also, the parametrization of the model is discussed. In Sec. III the numerical results of our simulations are presented, including a study of the influence of the coupling between the Q and B bands, the choice of basis set, and the final comparison to experiment. Furthermore, the interpretation of our results is discussed. Finally, in Sec. IV we summarize our results. Technical details pertaining to selection rules for absorption and LD spectra are included in the Appendix.

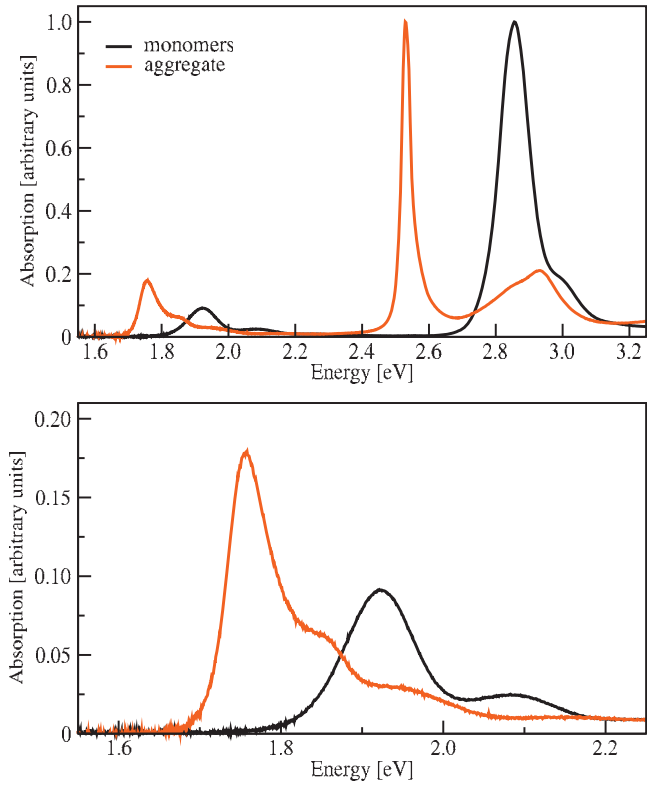

FIG. 2. Experimental spectra of various forms of $TPPS_4$ taken from Ref. 18. Black line: protonated monomers (at pH=4). Red line: aggregates (at pH =1). The lower plot shows a magnification of the Q band region.

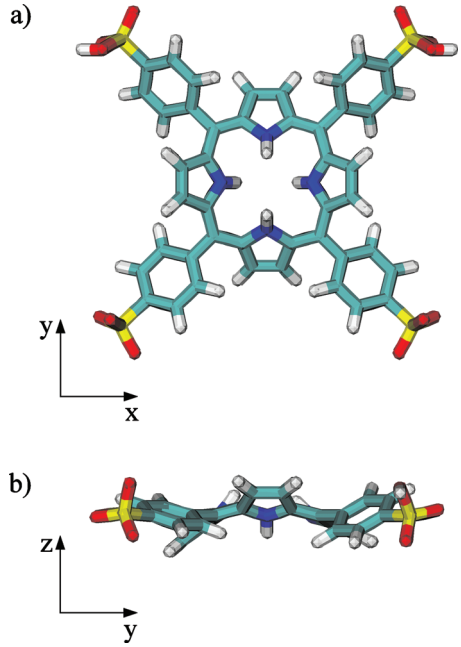

FIG. 3. Geometry of the zwitterionic form of $TPPS_4$ at pH=1. (a) Top view and (b) side view. The saddling distortion of the porphyrin ring is clearly visible in the side view. The orientations of the molecular axes x, y, and z are indicated by the arrows. The picture was prepared using VMD (Ref. 44).

II. MODEL

A. Aggregate geometry

The model for the aggregate geometry is essentially the same as in the recent paper by Vlaming *et al.*[18] and will be only briefly addressed here. The cylindrical arrangement of molecules is obtained by seamlessly rolling a planar aggregate onto the surface of a cylinder. The starting point for the construction of this arrangement is a square lattice with lattice vectors $\boldsymbol{a}_1 = a\hat{\boldsymbol{x}}'$ and $\boldsymbol{a}_2 = a\hat{\boldsymbol{z}}'$ and one $TPPS_4$ molecule per unit cell (see Fig. 4). The molecules are tilted out of plane in such a way, that the negatively charged sulphonate groups are placed above or below the positively charged centers of the neighboring molecules. This tilting is described by two subsequent rotations of the molecular (unprimed) coordinate system with respect to the lattice (primed) coordinate system. Before the rotations, the xy plane of the molecule coincides with the $x'z'$ lattice plane, the x and y molecular axes making the angles of $-45°$ and $+45°$ with $\boldsymbol{a}_1$, respectively. First, the molecular coordinates are rotated over an angle θ^+ around the $\hat{\boldsymbol{x}}+\hat{\boldsymbol{y}}$ vector. Next, they are rotated over an angle θ^- around the $\hat{\boldsymbol{x}}-\hat{\boldsymbol{y}}$ vector. The resulting planar structure is

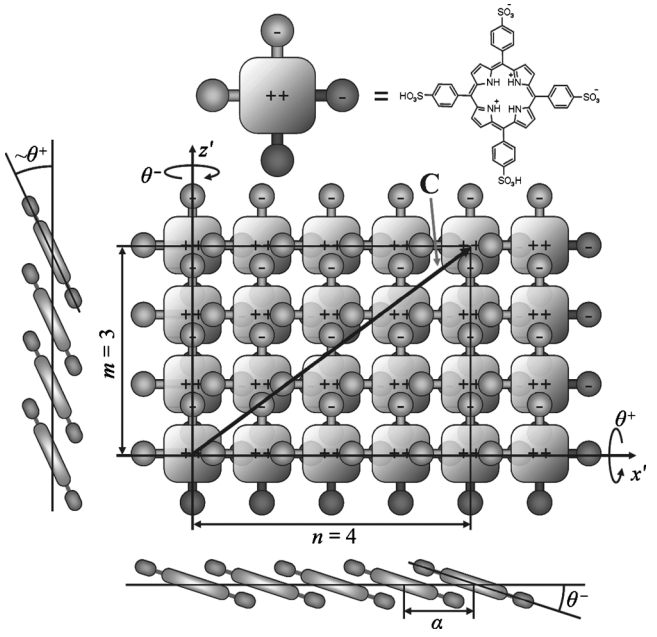

FIG. 4. Geometry of the planar aggregate before rolling it onto a cylindrical surface (taken from Ref. 18). The $TPPS_4$ monomers are drawn schematically, with their charged groups indicated by "+" and "−" signs. The lattice vectors $\boldsymbol{a}_1$ and $\boldsymbol{a}_2$ are of length a and are oriented along the x' and z' axes, respectively. The lighter parts of the molecules lie above the $x'z'$ plane, while the darker parts lie below it due to the tilting of the molecular xy plane over θ^+ and θ^-; this tilted structure is best seen in the side-views shown on the left and bottom side.

subsequently rolled along the chiral vector $\boldsymbol{C}$ so that its origin and end coincide. The axis of the thus formed cylinder is perpendicular to $\boldsymbol{C}$ and the circumference is equal to the length of $\boldsymbol{C}$.

As was shown in Ref. 23, a cylindrical aggregate can be treated as a stack of N_1 rings, composed of N_2 molecules each (see Fig. 5). The rings are stacked in the direction of the cylinder axis, the neighboring rings being separated by a distance h and rotated by a helical angle γ with respect to each other. Every molecule within the aggregate may be labeled by a pair of indices $\boldsymbol{n}=(n_1,n_2)$, with n_1 denoting the number of the ring and n_2 the number of the molecule within the ring. Two angles describe the orientation of the jth molecular transition dipole moment $\boldsymbol{\mu}_{\boldsymbol{n}j}$: α_j is the angle between the projection of $\boldsymbol{\mu}_{\boldsymbol{n}j}$ onto the ring plane and the local tangent to the ring, β_j is the angle between $\boldsymbol{\mu}_{\boldsymbol{n}j}$ and the cylinder axis. This "stack of rings" representation of the aggregate is particularly convenient for the determination of optical selection rules, since it allows one to make use of the cylindrical symmetry.

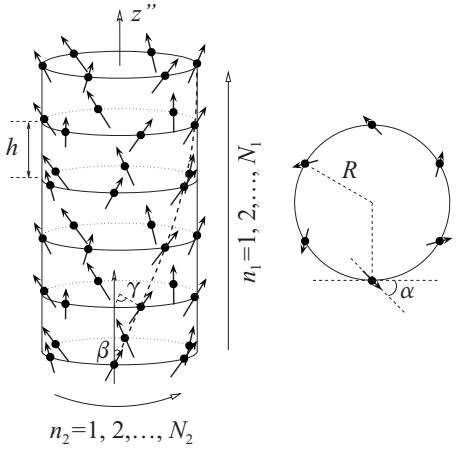

FIG. 5. Tubular aggregate represented as a stack of rings (taken from Ref. 23). The cylinder radius R, interring separation h, and angles γ, α, and β are indicated. The molecular transition dipole moments are represented as arrows; only one transition per molecule is drawn for clarity. On the right side a single ring is shown, together with projections of the transition dipole moments on its plane.

B. Hamiltonian and its eigenstates

We take into account four dipole-allowed electronic excited states (two pairs of degenerate states for the Q and the B band, respectively) and one totally symmetric harmonic internal vibration per porphyrin monomer. This effective vibrational mode mimics the influence of several high-frequency vibrations that couple to Q and B electronic transitions. We assume the vibrational potential to be harmonic and of the same curvature in the ground and electronic excited states; the positions of the minima of the potential curves for different states are displaced with respect to each other. In other words, we consider the case of linear vibronic coupling. Then, the aggregate Hamiltonian for one-exciton states reads

$$\hat{H} = \sum_{\boldsymbol{n},j} E_j |\boldsymbol{n}j\rangle\langle \boldsymbol{n}j| + \sum_{\boldsymbol{n},\boldsymbol{m}}{}' \sum_{j,l} J_{jl}(\boldsymbol{n}-\boldsymbol{m})|\boldsymbol{n}j\rangle\langle \boldsymbol{m}l| + \hbar\omega \sum_{\boldsymbol{n}} \hat{b}_{\boldsymbol{n}}^{\dagger}\hat{b}_{\boldsymbol{n}} + \hbar\omega \sum_{\boldsymbol{n},j} \lambda_j |\boldsymbol{n}j\rangle\langle \boldsymbol{n}j|(\hat{b}_{\boldsymbol{n}}^{\dagger} + \hat{b}_{\boldsymbol{n}}), \tag{1}$$

where $|\boldsymbol{n}j\rangle$ corresponds to the state of the aggregate with the molecule $\boldsymbol{n}$ in the jth electronic excited state and all the other molecules in the ground state (j being equal to Q_x, Q_y, B_x, or B_y) and E_j is the corresponding vertical excitation energy; $J_{jl}(\boldsymbol{n}-\boldsymbol{m})$ denotes the resonance interaction integral between the molecule $\boldsymbol{n}$ in the electronic excited state j and molecule $\boldsymbol{m}$ in the excited state l. The Bose operator $\hat{b}_{\boldsymbol{n}}^{\dagger}$ ($\hat{b}_{\boldsymbol{n}}$) creates (annihilates) a vibrational quantum of energy $\hbar\omega$ at molecule $\boldsymbol{n}$ in the potential of the electronic ground state. λ_j^2 corresponds to the Huang–Rhys factor (S) for the jth electronic transition.

In order to find the eigenstates of Hamiltonian (1) we employ the so called two-particle approximation.[24] This approximation is based on the observation that the one-exciton multiphonon basis set can be partitioned into subsets of n-particle states. An n-particle state describes a state of the aggregate in which one molecule is excited vibronically (i.e., both vibrationally and electronically) and $n-1$ molecules are excited vibrationally. Since only one-particle states are optically active and the Hamiltonian (1) couples different n-particle states only if n differs by not more than one, a natural hierarchy of coupling exists. Therefore one can construct an n-particle approximation by truncating the basis set to include only k-particle states for $k \leq n$.

In particular, within the two-particle approximation, the basis set is restricted to one- and two-particle states. We use the symbol $|\boldsymbol{n}j\tilde{v}^j\rangle$ to represent a one-particle state of the aggregate with molecule $\boldsymbol{n}$ in its jth electronic excited state and having v vibrational quanta in the displaced potential of this excited state, while all the other molecules of the aggregate are in the electronic and vibrational ground state. The two-particle state denoted by $|\boldsymbol{n}j\tilde{v}^j;\boldsymbol{n}+\boldsymbol{m}w\rangle$ corresponds to the situation when, apart from a vibronic excitation on molecule $\boldsymbol{n}$, there are w vibrational quanta in the potential of the electronic ground state located at molecule $\boldsymbol{n}+\boldsymbol{m}$ ($\boldsymbol{m}$ sites from the vibronically excited one). The tilde and the superscript j in $\tilde{v}^j$ are used to indicate the fact that v vibrational quanta are created in the potential of the electronic excited state j in contrast with the w quanta at molecule $\boldsymbol{n}+\boldsymbol{m}$, which are created in the potential of the electronic ground state.

The one-particle approximation corresponds to the (modified) strong vibronic coupling approximation.[30] Then, by allowing phonons to be located on electronically unexcited molecules, the two-particle approximation enables one to go beyond the strong coupling regime, toward the intermediate coupling strengths. At the same time it considerably reduces the size of the basis set compared to the full n-particle basis. However, even a relatively small nanotube contains several thousands of molecules as there are approximately 65 molecules per 10 Å of the nanotube length.[18] Thus the sheer number of molecules in the problem results in enormous number of two-particle states and further reduction of the basis set is necessary to make the calculations feasible. Therefore we introduce cutoffs for the number of phonons and for the exciton-phonon distance: the basis set contains only one- and two-particle states with total number of phonons not greater than $v_{\max}$ and only those two-particle states are included for which the distance between the vibronically and vibrationally excited molecules does not exceed $r_{\max}$. The values of $v_{\max}$ and $r_{\max}$ can be determined by subsequently increasing them, until convergence is reached. A similar approach was successfully used for sexithiophene crystals.[28,29]

In the absence of disorder, the aggregate's symmetry allows for further reduction of the numerical complexity and dictates optical selection rules. The cylindrical symmetry results in periodic boundary conditions for each ring. For long aggregates we may also impose periodic boundary conditions along the cylinder direction and use a Bloch-like form of the wave functions both in the ring (n_2) and cylinder (n_1) direction,

$$|\boldsymbol{k}j\tilde{v}^j\rangle = (N_1N_2)^{-1/2}\sum_{n_1,n_2} e^{i(k_1\phi_1n_1+k_2\phi_2n_2)}|\boldsymbol{n}j\tilde{v}^j\rangle, \tag{2}$$

$$|\boldsymbol{k}j\tilde{v}^j;\boldsymbol{m}w\rangle = (N_1N_2)^{-1/2}\sum_{n_1,n_2} e^{i(k_1\phi_1n_1+k_2\phi_2n_2)}|\boldsymbol{n}j\tilde{v}^j;\boldsymbol{n}+\boldsymbol{m}w\rangle, \tag{3}$$

where $\phi_i=2\pi/N_i$ and $k_i=0,\pm1,\pm2,\ldots,\pm(N_i/2-1),N_i/2$ for N_i even or $k_i=0,\pm1,\pm2,\cdots,\pm(N_i-1)/2$ for N_i odd. In this symmetry-adapted basis, the eigenvalue problem is split into N_1N_2 independent problems, one for each allowed value of the wavevector $\boldsymbol{k}=(k_1,k_2)$.

In the new basis the matrix elements of the Hamiltonian are given by

$$\langle\boldsymbol{k}j\tilde{v}^j|\hat{H}|\boldsymbol{k}l\tilde{u}^l\rangle = (E_j-\hbar\omega\lambda_j^2+\hbar\omega\tilde{v}^j)\delta_{jl}\delta_{\tilde{v}^j\tilde{u}^l}+J_{jl}(\boldsymbol{k})S_0^{\tilde{v}^j}S_0^{\tilde{u}^l},$$

$$\langle\boldsymbol{k}j\tilde{v}^j;\boldsymbol{m}w|\hat{H}|\boldsymbol{k}l\tilde{u}^l\rangle = J_{jl}(\boldsymbol{m})e^{i(k_1\phi_1m_1+k_2\phi_2m_2)}S_0^{\tilde{v}^j}S_w^{\tilde{u}^l}, \tag{4}$$

$$\begin{aligned}\langle\boldsymbol{k}j\tilde{v}^j;\boldsymbol{m}w|\hat{H}|\boldsymbol{k}l\tilde{u}^l;\boldsymbol{n}t\rangle &= [E_j-\hbar\omega\lambda_j^2+\hbar\omega(\tilde{v}^j+w)]\delta_{jl}\delta_{\boldsymbol{mn}}\delta_{\tilde{v}^j\tilde{u}^l}\delta_{wt}\\ &+J_{jl}(\boldsymbol{n})e^{i(k_1\phi_1m_1+k_2\phi_2m_2)}S_t^{\tilde{v}^j}S_w^{\tilde{u}^l}\delta_{\boldsymbol{m},-\boldsymbol{n}}\\ &+J_{jl}(\boldsymbol{n}-\boldsymbol{m})e^{i(k_1\phi_1(m_1-n_1)+k_2\phi_2(m_2-n_2))}S_0^{\tilde{v}^j}S_0^{\tilde{u}^l}\delta_{wt}(1-\delta_{\boldsymbol{mn}}),\end{aligned}$$

where $J_{jl}(\boldsymbol{k})=\Sigma'_{n_1,n_2}J_{jl}(\boldsymbol{n})\exp[-i(k_1\phi_1n_1+k_2\phi_2n_2)]$ and the summation is performed consistently with the periodic boundary conditions. $E_j-\hbar\omega\lambda_j^2$ is the adiabatic excitation energy to state j and $S_w^{\tilde{v}^j}$ is the overlap integral between the vibrational wave function for v phonons in the displaced potential of the jth electronic excited state and w phonons in the undisplaced potential of the electronic ground state. Matrix elements of the Hamiltonian between states of different wavevector vanish.

Now, for every value of the wavevector $\boldsymbol{k}$, the eigenstates of Hamiltonian (1) can be written as

$$|\boldsymbol{k}p\rangle = (N_1N_2)^{-1/2}\sum_{n_1,n_2} e^{i(k_1\phi_1n_1+k_2\phi_2n_2)} \times\left[\sum_{j,\tilde{v}^j} c_{j\tilde{v}^j}^{(p)}(\boldsymbol{k})|\boldsymbol{n}j\tilde{v}^j\rangle+\sum_{j,\tilde{v}^j,\boldsymbol{m},w} c_{j\tilde{v}^j\boldsymbol{m}w}^{(p)}(\boldsymbol{k})|\boldsymbol{n}j\tilde{v}^j;\boldsymbol{n}+\boldsymbol{m}w\rangle\right], \tag{5}$$

where the coefficients $c_{j\tilde{v}^j}^{(p)}(\boldsymbol{k})$ and $c_{j\tilde{v}^j\boldsymbol{m}w}^{(p)}(\boldsymbol{k})$ are components of the pth eigenvector of the Hamiltonian matrix Eq. (4) corresponding to one-particle and two-particle states, respectively. As the transitions from the vibrationless ground state to two-particle states carry no oscillator strength, the transition dipole moment from the overall (electronic and vibrational) ground state $|0\rangle$ to state $|\boldsymbol{k}p\rangle$ is solely determined by the one-particle contributions, and using the Condon approximation can be expressed as

$$\begin{aligned}\boldsymbol{\mu}_{\boldsymbol{k}p} &= \langle 0|\hat{\boldsymbol{\mu}}|\boldsymbol{k}p\rangle\\ &= (N_1N_2)^{-1/2}\sum_{n_1,n_2,j,\tilde{v}^j} e^{i(k_1\phi_1n_1+k_2\phi_2n_2)}c_{j\tilde{v}^j}^{(p)}(\boldsymbol{k})S_0^{\tilde{v}^j}\boldsymbol{\mu}_{\boldsymbol{n}j},\end{aligned} \tag{6}$$

where $\hat{\boldsymbol{\mu}}$ is the dipole moment operator of the aggregate, and $\boldsymbol{\mu}_{\boldsymbol{n}j}$ is the transition dipole moment to the jth electronic excited state on molecule $\boldsymbol{n}$. For the high-frequency vibrations, the thermal occupation of the vibrational excited states is negligible even at room temperature, and the absorption originates (almost) exclusively from the vibrationless ground state. Thus the transition dipole moments in Eq. (6) are sufficient to determine the absorption and LD spectra.

C. Optical spectra and selection rules

We calculate the isotropic absorption spectra as

$$A(E) = \sum_{kp} \langle |\boldsymbol{\mu}_{kp} \cdot \hat{\boldsymbol{e}}|^2 \rangle f_{kp}(E), \tag{7}$$

where $\langle \cdots \rangle$ denotes the average over the aggregate orientations with respect to the polarization $\hat{\boldsymbol{e}}$ of the incident light and $f_{kp}(E)$ is a line-shape function centered around the energy E_{kp} of state $|kp\rangle$. A Gaussian function of width σ_{kp},

$$f_{kp}(E) = \frac{1}{\sqrt{2\pi}\sigma_{kp}} \exp\left[-\frac{(E - E_{kp})^2}{2\sigma_{kp}^2} \right]. \tag{8}$$

is used throughout this paper, as for $TPPS_4$ nanotubes this choice turned out to give better reproduction of the experimental spectra than Lorentzian line-shape. The linear dichroism spectrum is calculated as the difference between the absorption for light polarized along the aggregate axis and perpendicular to it,

$$LD(E) = \sum_{kp} (|\boldsymbol{\mu}_{kp} \cdot \hat{\boldsymbol{e}}_{\parallel}|^2 - \langle |\boldsymbol{\mu}_{kp} \cdot \hat{\boldsymbol{e}}_{\perp}|^2 \rangle) f_{kp}(E), \tag{9}$$

where $\hat{\boldsymbol{e}}_{\parallel}$ and $\hat{\boldsymbol{e}}_{\perp}$ are the polarization vectors of light polarized parallel and perpendicular to the cylinder axis, respectively, and $\langle \cdots \rangle$ indicates the average over rotations of the aggregate around its axis.

The orientational averages in Eqs. (7) and (9) can be calculated analytically. The obtained expressions (see Appendix) are a straightforward generalization of earlier results for the purely excitonic model.[18,23] There are only three values of the wavevector $\boldsymbol{k}$ for which states can occur that contribute to the isotropic absorption and linear dichroism spectra, namely, $\boldsymbol{k}=\boldsymbol{0}$, $\boldsymbol{k}=(\gamma/\phi_1, 1)$, and $\boldsymbol{k}=(-\gamma/\phi_1, -1)$. Optically active states in the $\boldsymbol{k}=\boldsymbol{0}$ band have transition dipoles oriented along the cylinder axis, yielding positive contributions to the LD spectrum, while states in the $\boldsymbol{k}=\pm(\gamma/\phi_1, 1)$ band are polarized perpendicular to the cylinder axis and contribute a negative signal to the LD spectrum.

D. Parametrization

Our model contains a number of parameters that characterize the geometry of the aggregate, the molecular excitations, and the intermolecular interactions. Values (or at least estimates) of most of them can be obtained from independent experimental data, the few unknown ones are treated as fit parameters.

The diameter of the aggregate is known from cryo-EM experiments[18] to be equal to 179 ± 5 Å; we thus take the radius to be equal $R=90$ Å. The length of the chiral vector $\boldsymbol{C}$ is fixed by the cylinder radius via the relation $|\boldsymbol{C}|=2\pi R$. However, the rolling angle θ between $\boldsymbol{C}$ and lattice vector $\boldsymbol{a}_1$ is unknown, thus we treat it as a free parameter. From small-angle x-ray scattering[31,32] the lattice constant is found to be about 10 Å, while the previous theoretical modeling disregarding vibronic coupling yielded a value of $a=9.30$ Å upon fitting experimental spectra.[18] We take the latter value as a starting point, but allow for small variations during the fit procedure; it turns out that $a=9.30$ Å is optimal also for our model. The tilt angles θ^+ and θ^- were estimated to be in the range of $\pm 15°$–$25°$,[31] thus we treat them as almost free parameters. The positions and relative intensities of peaks in the calculated absorption and LD spectra turn out to be very sensitive to the values of the fit parameters (θ, θ^+, and θ^-). The correct reproduction of the experimental peak polarizations demands that the tilt angles θ^+ and θ^- have opposite signs. Their magnitude is fixed by the splitting between the two peaks in the absorption spectrum of the aggregate *B* band. The value of the rolling angle is set by the shape of the experimental LD spectrum, where no doublets (pairs of positive and negative peaks) are observed.[18] The best fit to the experimental spectra was obtained for tilt angles of $\theta^+ = -\theta^- = 24°$ and rolling angle $\theta = 45°$. The agreement of these angles with the previous study using a purely excitonic model[18] is within the range of one degree.

The values of the parameters pertaining to $TPPS_4$ monomers can be obtained from the monomer spectra (Fig. 2). The energy of a quantum of the effective vibration as well as the Huang–Rhys factor for the *Q* band were fitted to the vibronic progression in the experimental absorption spectrum of the monomer *Q* band,[18] yielding values of $\hbar\omega = 0.158$ eV and $\lambda_{Q_x}^2 = \lambda_{Q_y}^2 = 0.21$. For the *B* band, the resonance Raman data[33] yield the Huang–Rhys factor for the $\hbar\omega = 0.158$ eV vibration of $\lambda_{B_x}^2 = \lambda_{B_y}^2 = 0.01$ (we will refer to this set of parameters for the *B* band as "parametrization 1"). However, the monomer absorption spectrum[18] exhibits a shoulder. If this shoulder is treated as a vibronic replica of the *B* band, the fit to the absorption spectrum yields the energy of a vibrational quantum of 0.130 eV and $\lambda_{B_x}^2 = \lambda_{B_y}^2 = 0.26$ ("parametrization 2"). As discussed in the next section, in most of the calculations we disregard the vibronic coupling effects for the *B* band by setting $\lambda_{B_x}^2 = \lambda_{B_y}^2 = 0.00$.

The main peaks in the monomer absorption spectrum are found at 1.92 eV for the *Q* band and at 2.86 eV for the *B* band, respectively;[18] in our modeling we assumed the adiabatic excitation energies equal to $E_{Q_x} = E_{Q_y} = 1.84$ eV and $E_{B_x} = E_{B_y} = 2.86$ eV. The reduction of the *Q* band energy with respect to the experimental value for the monomers was needed for a proper reproduction of the aggregate *Q* band (this could not be obtained by varying the free parameters describing the aggregate geometry). This solution-to-aggregate redshift is due to those interactions that are not included in our modeling, the main contribution being probably the influence of charge-transfer states which are located in the energetic proximity to the *Q* band as a result of the close packing of the molecules in the aggregate (the distance between the pyrrole rings of neighboring molecules is below 3 Å). The transition dipole moment for the degenerate B_x and B_y transitions was previously evaluated from spectroscopic data as 2.35 eÅ (11.3 D).[18,34] Based on the ratio of the integrated absorbance of the *Q* band relative to the *B* band, we estimate the transition dipole moment for degenerate Q_x and Q_y transitions as 0.91 eÅ (4.4 D).

Due to the proximity of neighboring molecules within the aggregate, the point-dipole approximation for calculating the resonance integrals fails.[6,35–37] We thus use the extended dipole representation: every transition dipole moment is represented by a pair of charges $+q$ and $-q$ separated by a dis-

tance L. Values and positions of those charges are chosen in such a way, that the dipole moment qL correctly reproduces the magnitude, orientation, and position of a molecular transition dipole moment. The resonance interaction $J_{ij}(\boldsymbol{n}-\boldsymbol{m})$ is then calculated as Coulomb interaction between two pairs of charges representing the transition dipole moments to the ith electronic excited state of molecule $\boldsymbol{n}$ and the jth state of molecule $\boldsymbol{m}$. We assume that the charge separation L is equal to 5 Å, a value roughly corresponding to the diameter of the porphyrin ring. To obtain the proper values of the transition dipole moments, the values of the charges q were taken as 0.470 e for the B_x and B_y transitions and 0.182 e for the Q_x and Q_y transitions, respectively.

The remaining model parameters are the linewidths $\sigma_{\boldsymbol{k}p}$. Their values were fitted to reproduce the experimental spectra of the aggregate. We used four values of $\sigma_{\boldsymbol{k}p}$, depending on the energy of the state $|\boldsymbol{k}p\rangle$: (i) 0.030 eV for states of energy smaller than 1.8 eV, (ii) 0.035 eV for states of energy from 1.8 to 2.25 eV, (iii) 0.014 eV for states of energy from 2.25 to 2.7 eV, (iv) and 0.090 eV for states of energy higher than 2.7 eV. The linewidths reflect the combined effect of variation in the lifetimes of the absorbing states and different values of the disorder for the Q and B band. They are introduced as phenomenological fit parameters. Modeling the lifetime-imposed part of these widths through scattering on low-frequency vibrations[38] is the topic of current research.

III. RESULTS

A. Coupling between Q and B bands

Due to the large separation of the Q and B bands in the monomer absorption spectrum (of almost 1 eV), one may be tempted to neglect the coupling between them. We performed test calculations neglecting the mixing of both bands and compared them with the results obtained when the mixing was fully taken into account (all the other parameters of the model were kept the same for both types of calculations). When the Q-B coupling is disregarded, no physically reasonable set of parameters allows for the correct reproduction of the experimental absorption spectrum of the Q band (see red and black curves in Fig. 6). The splitting between the two lowest-energy peaks within the Q band (experimentally found at 1.76 and 1.85 eV) is significantly underestimated with respect to the experimental value, moreover, the intensity distribution between them is incorrect. On the other hand, when the mixing of the Q and B bands is taken into account (green and blue curves in Fig. 6) the lowest-energy peak of the Q band is redshifted and gains intensity, while the position and magnitude of the second peak remain almost unchanged. This yields correct splittings and intensity ratios in the Q band absorption, irrespective which parametrization (1 or 2) is used for the B-band vibronic coupling.

The apparent sensitivity of the lowest-energy peak to the Q-B coupling, accompanied by the insensitivity of the second-lowest peak, can be explained based on the geometry of the aggregate and the long-range character of dipole-dipole interactions. For simplicity, we limit the discussion here to the sums of resonance integrals $J_{ij}(\boldsymbol{k})$; when multiplied by the vibrational overlap factors they give the couplings within the one-particle subspaces for every value of wavevector [see Eq. (4)]. As discussed later on (Sec. III C), the one-particle level of description works very well for the two lowest-energy peaks within the aggregate's Q band absorption.

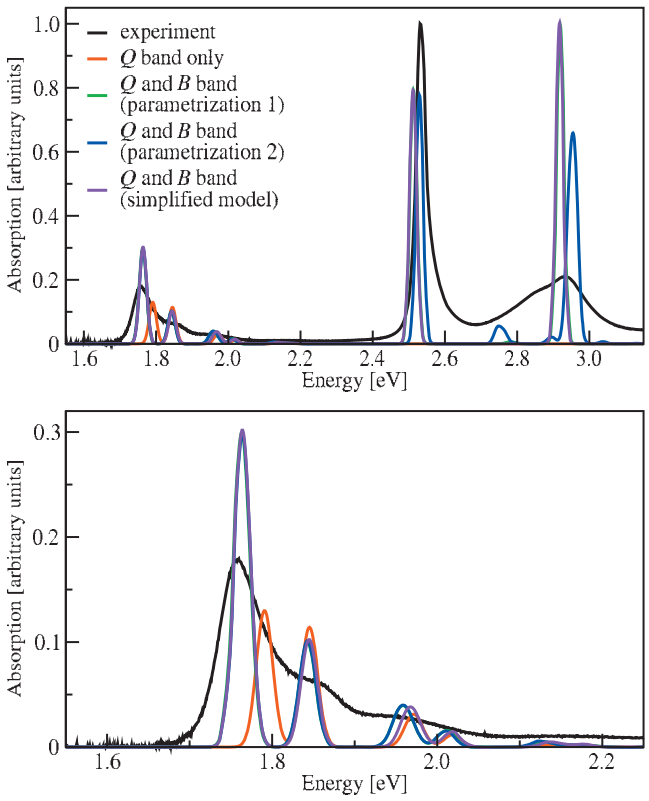

FIG. 6. Isotropic absorption spectra of the porphyrin nanotubes calculated with and without the inclusion of the B band in the model. Red line: model taking into account only the Q band. Green and blue lines: models taking into account both Q and B bands (parametrizations 1 and 2, respectively). The cutoffs were set to $v_{\max}=2$ and $r_{\max}=a$ (lattice constant). Purple line: the spectrum calculated with the simplified model for the B band; the Huang–Rhys parameter for the B band is set to zero, so that the purely excitonic basis set is used for this band, while the two-particle basis set is used for the Q band. Green, blue, and purple lines are superimposed in some regions. Narrow peak widths ($\sigma=0.01$ eV) are used so that the structure of the Q band is clearly visible. Experimental results from Ref. 18 are plotted in black. The lower plot shows a magnification of the Q band region.

For the geometric parameters that we found for the $TPPS_4$ aggregates, the Q_x and B_x monomer excited states are polarized mostly parallel to the cylinder axis. The angle that the transition dipole moment $\boldsymbol{\mu}_{Q_x(B_x)}$ makes with the long axis of the aggregate is then equal to 175.0°, while the angle between the projection of $\boldsymbol{\mu}_{Q_x(B_x)}$ onto the plane of the ring and the local tangent to the ring is 16.7°. On the other hand, the transition dipole moments for the Q_y and B_y states are almost perpendicular to the axis of the cylinder, the corresponding angles being equal to $\beta_{Q_y(B_y)}=85.2°$ and $\alpha_{Q_y(B_y)}=33.5°$. This leads to differences both in the magnitude and the sign of the sums of resonance integrals $J_{ij}(\boldsymbol{k})$ that couple molecular excitations of different polarizations; selected values for $\boldsymbol{k}=\boldsymbol{0}$ are presented in Table I; in case of $\boldsymbol{k}=\pm(\gamma/\phi_1,1)$ results are qualitatively the same. Clearly, the coupling between the Q_x and B_x transitions is an order of magnitude larger than between Q_y and B_y excitations and has

TABLE I. Values of the sums of resonance integrals $J_{ij}(\mathbf{k}=\mathbf{0})$ between the Q and B states. Summation was performed consistent with periodic boundary conditions over 117 rings of 43 molecules each (5031 molecules). The coupling between states polarized along the molecular x axis is an order of magnitude stronger than between y-polarized states; the coupling between states of different polarizations is negligible. Similar results were obtained for $J_{ij}(\mathbf{k}=\pm(\gamma/\phi_1,1))$.

Integral	Value (eV)
$J_{Q_xB_x}$	−0.147
$J_{Q_xB_y}$	0.006
$J_{Q_yB_x}$	0.006
$J_{Q_yB_y}$	0.013

an opposite sign. The coupling between x- and y-polarized states is even weaker than between y-polarized states.

The differences in the coupling strengths for the states of different polarizations have a pronounced effect on the spectra. The lowest-energy peak in the absorption spectrum originates mostly from the Q_x molecular transitions; the relatively strong coupling with B_x excitations shifts its position toward the red and results in intensity borrowing from the intense B_x states. This is in perfect agreement with the results obtained for porphyrin aggregates of simpler geometry,[39,40] showing that the coupling between transitions of the same polarization plays an important role, in spite of the relatively large energy separation of the Q and B bands. The situation is different for the second-lowest peak in the Q band absorption, to which Q_y states contribute most. As their coupling with B_y (and B_x) excitations is weak, the shift in the position and change in the intensity due to the coupling with B states is negligible.

Because we are here concerned with the Q band absorption and LD spectra, and both parametrizations for the B band yield very similar results for the Q band, we tested the performance of a simplified model. This model fully takes into account the vibronic coupling for the Q band and the excitonic coupling between Q and B bands, but neglects the effects of vibronic coupling for the B band. This corresponds to setting the Huang–Rhys parameter for the B band to zero ($\lambda^2_{B_x}=\lambda^2_{B_y}=0$). Then, the Hamiltonian (1) couples the Q band states only to the undressed B band excitons (B band zero-phonon one-particle states); all the other B band states (one- and more-phonon, both one- and two-particle) carry no oscillator strength and are decoupled from all optically active states. The simplified model works extremely well (purple curve in Fig. 6) for the Q band region. Parametrizations 1 and 2 as well as the simplified model all yield very similar spectra for the Q band region, the difference being only a small blueshift (0.01 eV) of the third peak in the simplified model with respect to parametrizations 1 and 2. The situation is different in the B band region of the spectrum. The simplified model yields almost identical results as parametrization 1, as is expected from the fact that for this parametrization the Huang–Rhys factor is only 0.01, implying that setting it to zero (simplified model) should not give noticeable changes. Parametrization 2 (blue curve in Fig. 6) yields main peaks within the B band that are slightly blueshifted with respect to the results of the two other models; it also predicts additional peaks at 2.75, 2.89, and 3.04 eV (vibronic replicas). Due to the large linewidth of the second peak in the absorption spectrum of the B band, all three models yield sufficiently good reproduction of the experimental data. Thus, for further calculations we used the simplified model, as it is computationally less expensive than the other two.

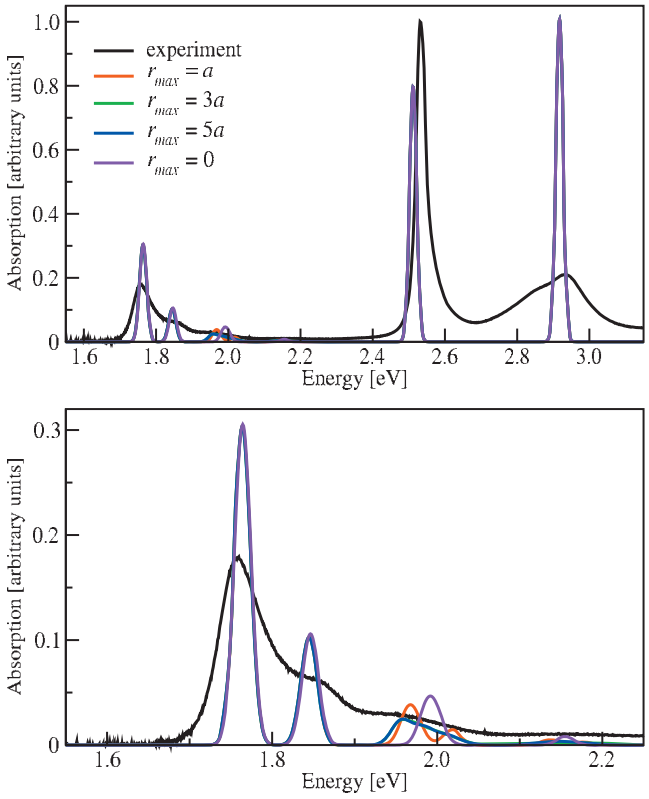

FIG. 7. Isotropic absorption spectra of the porphyrin nanotubes calculated using the simplified model for the B band. The phonon number cutoff was set to $v_{\max}=2$. Purple line: one-particle approximation, red, green, and blue lines, two-particle approximation with exciton-phonon distance cutoff $r_{\max}$ equal to one, three, and five lattice constants (a), respectively. Thanks to a good convergence with increasing $r_{\max}$ the lines of different colors overlap to a large extent; especially the spectra for $r_{\max}=3a$ and $r_{\max}=5a$ (green and blue lines) are almost indistinguishable. The lower plot shows a magnification of the Q band region.

B. Choice of basis set: convergence tests

In order to find the values of basis set cutoff parameters, we performed a series of calculations with increasing values of $v_{\max}$ and $r_{\max}$. For a wide range of parameter sets tested, the convergence with respect to phonon number cutoff was reached already for $v_{\max}=2$. This value was used for all subsequent calculations. The convergence with respect to the exciton-phonon distance cutoff is also good—spectra stop to change once $r_{\max}$ reaches the value of three lattice constants (27.9 Å, see Fig. 7). The increase of $r_{\max}$ from one to three lattice constants leads to minute changes in the spectra, observed only in the region of the third peak in the Q band, where two separate peaks merge into one asymmetric band.

The comparison of the spectra from the two-particle approximation with the results obtained from the one-particle approximation ($r_{\max}=0$ in Fig. 7) shows that this relatively

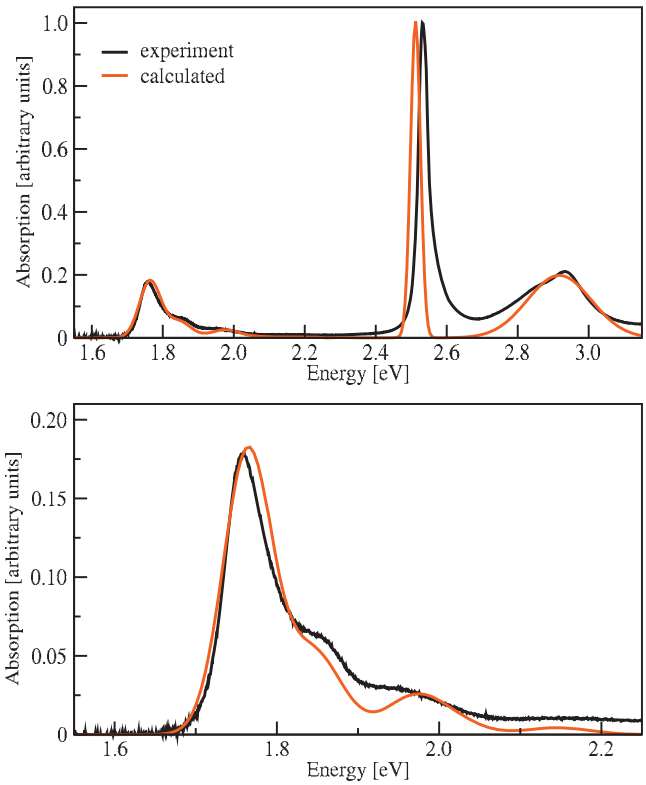

FIG. 8. Isotropic absorption spectrum of the porphyrin nanotubes calculated using the two-particle approximation for the Q band states and the purely excitonic basis set for the B band. The cutoffs were set to $v_{max}=2$ and $r_{max}=3a$ (27.9 Å). The peak widths were fitted to the experimental spectrum. The lower plot shows a magnification of the Q band region.

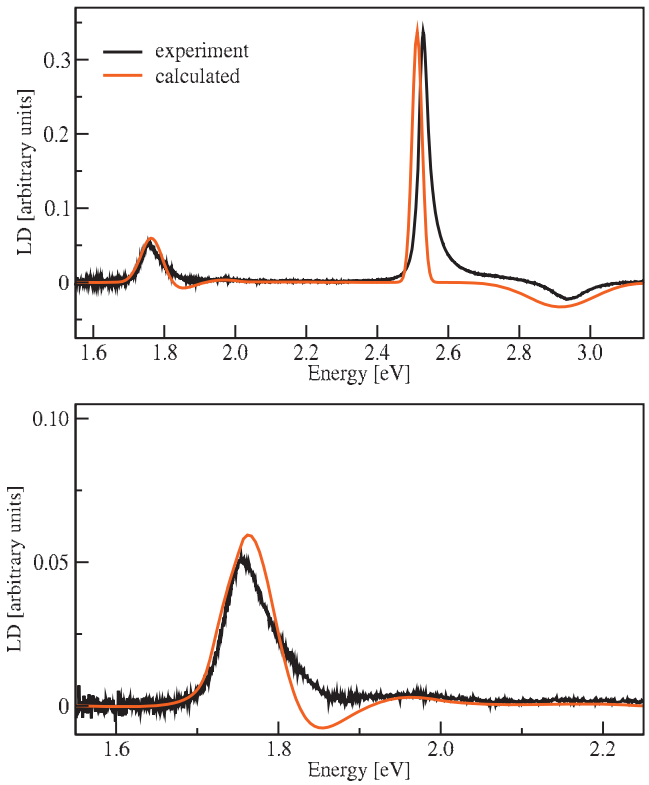

FIG. 9. Linear dichroism spectra of the porphyrin nanotubes calculated using the two-particle approximation for the Q band states and the purely excitonic basis set for the B band. All parameters used were exactly the same as for the absorption spectra from Fig. 8.

simple level of theory works extremely well. The deviations from two-particle approximation results can again be seen only within the third peak of the Q band absorption. This suggests that the convergence of the n-particle expansion is very good for the set of parameters corresponding to porphyrin nanotubes and that for most of the spectrum even the least computationally expensive one-particle approximation can be used.

C. Interpretation

Figures 8 and 9 present the isotropic absorption and linear dichroism spectra for porphyrin nanotubes obtained in the two-particle approximation, using the set of parameters described in the previous section and linewidths fitted to the experimental spectra. Inspection of the eigenstates contributing to the aggregate Q band absorption shows a surprising fact—the lowest-energy (1.76 eV) and the second-lowest (1.85 eV) peaks in the absorption spectrum of the aggregate Q band are not the $0\rightarrow0$ transition and its $0\rightarrow1$ vibronic replica.

The intermolecular interactions within the aggregate split the degenerate molecular excitations into pairs of states. The mechanism of this so-called Bethe splitting[41,42] is similar to the one that gives rise to the Davydov splitting[43] of nondegenerate molecular terms due to the presence of several molecules in the unit cell. As a result of the aggregate's geometry discussed in Sec. III A, the x-polarized molecular states give rise to the redshifted lower Bethe components (both in the Q and B bands), while the y-polarized states contribute to the upper Bethe component. The small admixtures of other states do not change this qualitative picture.

Over 99% of the intensity of the first absorption peak within the Q band is carried by one state, polarized along the aggregate axis. It is best described as the $0\rightarrow0$ transition associated with the lower Bethe component of the Q band for $\boldsymbol{k}=(0,0)$ (94% contribution to the state under consideration). The admixture of the B band is small (3.7%), but as discussed in Sec. III A, it considerably affects both the energy and the transition dipole moment of the state at hand. The lower components of the $\boldsymbol{k}=\pm(\gamma/\phi_1,1)$ transitions, polarized perpendicular to the aggregate axis, are also located in the energy region of the first peak. However, as the Q_x molecular states are polarized almost parallel to the aggregate axis, these states carry almost no oscillator strength, and their contributions to absorption and LD spectra are negligible.

The second peak originates from the $0\rightarrow0$ vibronic transition of the upper Bethe component. Due to the geometry of the aggregate, the contribution from $\boldsymbol{k}=(0,0)$ is insignificant here, and the intensity is carried by the degenerate $\boldsymbol{k}=\pm(\gamma/\phi_1,1)$ transitions polarized perpendicular to the aggregate axis. Also the mixing with the B band is negligible (the contribution from the B band being smaller than 0.04%), which, as discussed earlier, is the reason why the intensity and location of the second peak do not change when the coupling to the B band is not included in the model.

The above observations explain the good convergence of the calculated spectra with respect to the cutoff parameter

r_{max}. The contributions from the $0 \rightarrow 0$ transitions to the two lowest-energy peaks in the Q band absorption and both peaks in the B band absorption are over 90%. Since the $0 \rightarrow 0$ excitations are correctly represented in the one-particle basis set, the number of two-particle states included in the basis (governed by the r_{max} parameter) has only a small influence on those peaks. On the other hand, for the correct description of one-phonon excitations the two-particle states must be included in the basis set, to allow the phonon to be located on another molecule than the exciton. This can be observed for the third peak in the Q band absorption, which arises from the overlapping first vibronic replicas of the peaks at 1.76 and 1.85 eV. Many states of different polarizations and small oscillator strengths contribute to the absorption in the energy region of the third Q band peak. In the saturated basis set ($r_{max}=3a$) those states have predominantly two-particle character, the contribution of two-particle states being at least 75%. This explains why the shape of the third peak is sensitive to the size of the basis set used in the calculations—smaller basis sets are not able to correctly reproduce the phonon cloud surrounding the exciton.

We note that a discrepancy between the theoretical and experimental LD spectra still exists in the region corresponding to the second peak in the Q-band absorption (around 1.85 eV). Our calculations yield a small negative signal, while the experimentally observed LD is small but positive. This is probably due to the fact that our model disregards low-frequency vibrational modes, such as the 242 and 317 cm^{-1} vibrations of the $TPPS_4$ monomer.[33] Incorporation of those modes into the model could lead to a situation similar to the one observed within our model for the third peak in the absorption spectrum of the Q band (around 1.95 eV), where many states of different polarizations contribute to the isotropic absorption spectrum, but do not lead to an observable LD signal.

IV. CONCLUSIONS

We modeled the optical spectra of self-assembled porphyrin nanotubes taking into account the electronic coupling within and between the Q and B bands as well as vibronic coupling to one (effective) high-frequency molecular vibration. We used the same model for the aggregate geometry as in the earlier work by Vlaming *et al.*,[18] where a simple electronic model was assumed by disregarding coupling between the Q and B bands as well as the coupling to vibrations. From fitting experimental absorption and LD spectra, we obtained essentially the same values of the parameters defining the geometry of the aggregate as in Ref. 18, which are the tilt and chiral angles and the lattice constant. This shows that the purely excitonic model used previously allowed to extract the structural information from spectral data, in spite of being unable to correctly reproduce and interpret the fine structure of the Q band absorption.

The step forward in our work is that by adding the vibronic coupling and the coupling between the Q and B bands, we were able to reproduce the spectral structure in the Q band. This allows for a solid interpretation of this structure. Specifically, from our calculations it turned out that the first two peaks in the Q band absorption spectrum are the $0 \rightarrow 0$ transitions, respectively, of the lower Bethe component for the subband with perpendicular wavenumber 0 and the upper Bethe component for the subband with perpendicular wavenumber ± 1. Moreover we showed that the electronic coupling between Q and B bands, often neglected in the modeling of porphyrin systems, although being weak, is crucial for a correct reproduction of optical spectra, in accordance with the earlier results of Gülen and co-workers.[39,40] Finally, we showed that the vibronic coupling to the high-frequency vibrational mode is important for the reproduction of the detailed shape of the absorption spectrum, specifically in the region of the first vibronic replica, that is the third peak in the Q band absorption spectrum. Interestingly, the shape of the Q band turned out to be independent of the level of description of the vibronic coupling in the B band. The three different models that we introduced, namely, the simplified model with no vibronic coupling in the B band, the model with weak coupling to the same vibration as for the Q band, as well as the one with an intermediate coupling to another vibration, have all resulted in almost identical spectra of the Q band region.

Apart from the coupling of excitons to the high-frequency intramolecular vibrational modes that we considered here, it would be interesting to include the weak coupling to low frequency vibrational modes in the environment, which leads to relaxation within (and between) exciton bands. Combined with the treatment of the static disorder, this would allow to properly account for the homogenous and inhomogeneous line widths.[38] Such an investigation is currently under way in our group.

ACKNOWLEDGMENTS

A.S. acknowledges The Netherlands Organisation for Scientific Research (NWO) for support through a Rubicon grant. Some of the numerical calculations were carried out at the Academic Computer Center in Gdańsk.

APPENDIX: SELECTION RULES

The cylindrical symmetry of the aggregates considered in this paper allows for analytical calculation of the orientational averages in Eqs. (7) and (9). This is conveniently done using the representation of the aggregate as a stack of rings, with every molecule identified by a pair of indices $\boldsymbol{n}=(n_1,n_2)$, denoting the number of the ring the molecule lies on and its location within the ring, respectively. The distance between the rings is denoted by h and neighboring rings are rotated with respect to each other over a helical angle γ. The orientation of the molecular transition dipole moments $\boldsymbol{\mu}_{\boldsymbol{n}j}$ is specified by two angles: the angle between the projection of $\boldsymbol{\mu}_{\boldsymbol{n}j}$ onto the ring plane and the local tangent to the ring denoted by α_j and the angle between $\boldsymbol{\mu}_{\boldsymbol{n}j}$ and the cylinder axis denoted by β_j (for details see Ref. 23):

$$\boldsymbol{\mu}_{\boldsymbol{n}j} = (-\mu_j \sin\beta_j \sin(n_2\phi_2 + n_1\gamma - \alpha_j), \mu_j \sin\beta_j \cos(n_2\phi_2 + n_1\gamma - \alpha_j), \mu_j \cos\beta_j). \quad \text{(A1)}$$

Then the isotropic absorption intensity of state $|\boldsymbol{k}p\rangle$ is given by

$$\langle|\boldsymbol{\mu}_{kp}\cdot\hat{\boldsymbol{e}}|^2\rangle = \frac{N}{3}\sum_{jl\tilde{v}^j\tilde{u}^l} S_0^{\tilde{v}^j} S_0^{\tilde{u}^l} c_{l\tilde{u}^l}^{(p)*}(\boldsymbol{k}) c_{j\tilde{v}^j}^{(p)}(\boldsymbol{k})\mu_j\mu_l \times\Bigg(\cos\beta_j\cos\beta_l\delta_{\boldsymbol{k},\boldsymbol{0}} + \frac{1}{2}\sin\beta_j\sin\beta_l e^{-i(\alpha_j-\alpha_l)}\delta_{\boldsymbol{k},-(\gamma/\phi_1,1)} + \frac{1}{2}\sin\beta_j\sin\beta_l e^{i(\alpha_j-\alpha_l)}\delta_{\boldsymbol{k},(\gamma/\phi_1,1)}\Bigg), \tag{A2}$$

where $N=N_1N_2$ is the total number of molecules in the aggregate. Analogously, the linear dichroism strength is

$$(|\boldsymbol{\mu}_{kp}\cdot\hat{\boldsymbol{e}}_{\parallel}|^2 - \langle|\boldsymbol{\mu}_{kp}\cdot\hat{\boldsymbol{e}}_{\perp}|^2\rangle) = N\sum_{jl\tilde{v}^j\tilde{u}^l} S_0^{\tilde{v}^j} S_0^{\tilde{u}^l} c_{l\tilde{u}^l}^{(p)*}(\boldsymbol{k}) c_{j\tilde{v}^j}^{(p)}(\boldsymbol{k})\mu_j\mu_l \times\Bigg(\cos\beta_j\cos\beta_l\delta_{\boldsymbol{k},\boldsymbol{0}} - \frac{1}{4}\sin\beta_j\sin\beta_l e^{-i(\alpha_j-\alpha_l)}\delta_{\boldsymbol{k},-(\gamma/\phi_1,1)} - \frac{1}{4}\sin\beta_j\sin\beta_l e^{i(\alpha_j-\alpha_l)}\delta_{\boldsymbol{k},(\gamma/\phi_1,1)}\Bigg). \tag{A3}$$

[1] A. Pawlik, S. Kirstein, U. DeRossi, and S. Daehne, J. Phys. Chem. B **101**, 5646 (1997).
[2] S. S. Lampoura, C. Spitz, S. Dähne, J. Knoester, and K. Duppen, J. Phys. Chem. B **106**, 3103 (2002).
[3] C. Spitz, J. Knoester, A. Ouart, and S. Daehne, Chem. Phys. **275**, 271 (2002).
[4] L. Kelbauskas, S. Bagdonas, W. Dietel, and R. Rotomskis, J. Lumin. **101**, 253 (2003).
[5] J. Pšenčík, Y.-Z. Ma, J. B. Arellano, J. Hála, and T. Gillbro, Biophys. J. **84**, 1161 (2003).
[6] C. Didraga, A. Pugžlys, P. R. Hania, H. von Berlepsch, K. Duppen, and J. Knoester, J. Phys. Chem. B **108**, 14976 (2004).
[7] A. D. Schwab, D. E. Smith, B. Bond-Watts, D. E. Johnston, J. Hone, A. T. Johnson, J. C. de Paula, and W. F. Smith, Nano Lett. **4**, 1261 (2004).
[8] F. J. M. Hoeben, P. Jonkheijm, E. W. Meijer, and A. P. H. J. Schenning, Chem. Rev. (Washington, D.C.) **105**, 1491 (2005).
[9] E. Lang, A. Sorokin, M. Drechsler, Y. V. Malyukin, and J. Köhler, Nano Lett. **5**, 2635 (2005).
[10] E. Collini, C. Ferrante, and R. Bozio, J. Phys. Chem. B **109**, 2 (2005).
[11] Y. Yamamoto, T. Fukushima, Y. Suna, N. Ishii, A. Saeki, S. Seki, S. Tagawa, M. Taniguchi, T. Kawai, and T. Aida, Science **314**, 1761 (2006).
[12] C. Röger, M. G. Müller, M. Lysetska, Y. Miloslavina, A. R. Holzwarth, and F. Würthner, J. Am. Chem. Soc. **128**, 6542 (2006).
[13] H. von Berlepsch, S. Kirstein, R. Hania, A. Pugžlys, and C. Böttcher, J. Phys. Chem. B **111**, 1701 (2007).
[14] A. Eisfeld, R. Kniprath, and J. S. Briggs, J. Chem. Phys. **126**, 104904 (2007).
[15] C. Röger, Y. Miloslavina, D. Brunner, A. R. Holzwarth, and F. Würthner, J. Am. Chem. Soc. **130**, 5929 (2008).
[16] D. M. Eisele, J. Knoester, S. Kirstein, J. P. Rabe, and D. A. Vanden Bout, Nat. Nanotechnol. **4**, 658 (2009).
[17] A. Nemeth, F. Milota, J. Sperling, S. Abramovicius, D. Mukamel, and H. F. Kauffmann, Chem. Phys. Lett. **469**, 130 (2009).
[18] S. M. Vlaming, R. Augulis, M. C. A. Stuart, J. Knoester, and P. H. M. van Loosdrecht, J. Phys. Chem. B **113**, 2273 (2009).
[19] S. Ganapathy, G. T. Oostergetel, P. K. Wawrzyniak, M. Reus, A. Gomez Maqueo Chew, F. Buda, E. J. Boekema, D. A. Bryant, A. R. Holzwarth, and H. J. M. de Groot, Proc. Natl. Acad. Sci. U.S.A. **106**, 8525 (2009).
[20] R. Improta, C. Ferrante, R. Bozio, and V. Barone, Phys. Chem. Chem. Phys. **11**, 4664 (2009).
[21] A. Stone and E. B. Fleischer, J. Am. Chem. Soc. **90**, 2735 (1968).
[22] B. Cheng, O. Q. Munro, H. M. Marques, and W. R. Scheidt, J. Am. Chem. Soc. **119**, 10732 (1997).
[23] C. Didraga, J. A. Klugkist, and J. Knoester, J. Phys. Chem. B **106**, 11474 (2002).
[24] M. R. Philpott, J. Chem. Phys. **55**, 2039 (1971).
[25] F. C. Spano, J. Chem. Phys. **116**, 5877 (2002).
[26] Z. Zhao and F. C. Spano, J. Chem. Phys. **122**, 114701 (2005).
[27] F. C. Spano, Annu. Rev. Phys. Chem. **57**, 217 (2006).
[28] A. Stradomska and P. Petelenz, J. Chem. Phys. **130**, 094705 (2009).
[29] A. Stradomska and P. Petelenz, J. Chem. Phys. **131**, 044507 (2009).
[30] M. Andrzejak and P. Petelenz, Chem. Phys. **335**, 155 (2007).
[31] R. Rubires, J.-A. Farrera, and J. M. Ribó, Chem.-Eur. J. **7**, 436 (2001).
[32] S. C. M. Gandini, E. L. Gelamo, R. Itri, and M. Tabak, Biophys. J. **85**, 1259 (2003).
[33] D.-M. Chen, T. He, D.-F. Cong, Y.-H. Zhang, and F.-C. Liu, J. Phys. Chem. A **105**, 3981 (2001).
[34] R. F. Pasternack, C. Fleming, S. Herring, P. J. Collings, J. dePaula, G. DeCastro, and E. Gibbs, Biophys. J. **79**, 550 (2000).
[35] G. D. Scholes, Annu. Rev. Phys. Chem. **54**, 57 (2003).
[36] V. May and O. Kühn, *Charge and Energy Transfer Dynamics in Molecular Systems* (Wiley-VCH, Berlin, 2000).
[37] J. Gierschner, Y.-S. Huang, B. Van Averbeke, J. Cornil, R. H. Friend, and D. Beljonne, J. Chem. Phys. **130**, 044105 (2009).
[38] D. J. Heijs, V. A. Malyshev, and J. Knoester, Phys. Rev. Lett. **95**, 177402 (2005).
[39] H. Yıldırım, E. İ. İşeri, and D. Gülen, Chem. Phys. Lett. **391**, 302 (2004).
[40] D. Gülen, Photosynth. Res. **87**, 205 (2006).
[41] V. M. Agranovich, *Theory of Excitons* (Nauka, Moscow, 1968), (in Russian).
[42] H. Bethe, Ann. Phys. **395**, 133 (1929).
[43] A. S. Davydov, *Theory of Molecular Excitons* (McGraw-Hill, New York, 1962).
[44] W. Humphrey, A. Dalke, and K. Schulten, J. Mol. Graphics **14**, 33 (1996).